

1      **Better constraining the geometry of faults in the**  
2      **Charlevoix Seismic Zone**

3      **Oluwaseun Idowu Fadugba<sup>1</sup>, Charles Langston<sup>1</sup>, Christine A. Powell<sup>1</sup>, and**  
4      **Eunseo Choi<sup>1</sup>**

5      <sup>1</sup>Center for Earthquake Research and Information, The University of Memphis, Memphis, TN 38152

6      **Key Points:**

- 7      • The first fault dips at an angle of  $60^\circ$  while the other two main rift faults dip at  
8       $44^\circ$  and  $43^\circ$ , respectively. These fault geometries match the work by Powell and  
9      Lamontagne (2017).
- 10     • The rift faults show a more complicated geometry than the simple three-faults model  
11     in previous works, especially within the crater region.
- 12     • The rift fault to the northwest of the crater changes in strike and dip. The fault  
13     dips about  $60^\circ\text{SE}$  outside the crater, but has shallower dips of about  $33.4^\circ$  and  
14      $34.8^\circ$  within the crater.

---

Corresponding author: Oluwaseun Idowu Fadugba, [ifadugba@memphis.edu](mailto:ifadugba@memphis.edu)

**Abstract**

The Charlevoix Seismic Zone (CSZ) is located along the early Paleozoic St. Lawrence rift zone in southeastern Quebec at the location of a major Devonian impact structure. The impact structure superimposed three major basement faults trending approximately N35°E. Previous work suggests two sets of geometries for the rift faults. One set has a uniform dip of 70°SE for all three faults while the other has 65°, 40°, and 40°SE, from north to south, respectively. Visual estimation of fault planes from over 1300 relocated hypocenters in the CSZ suggests more complex fault geometry. We apply a cumulative distribution of volume (CDV) of tetrahedra defined by closest neighbor events to remove unclustered hypocenters. The declustering algorithm involves comparing the CDV in the natural catalog to that of a randomized catalog within a spatial domain similar to the seismic zone. We apply a modified version of the Optimal Anisotropic Dynamic Clustering (OADC) algorithm to model realistic fault planes that best fit the clustered hypocenters. OADC method is a generalization of the k-means method using randomly-seeded planes to partition hypocenters into clusters. OADC uses the eigenvalue-eigenvector analysis of the covariance of hypocenter locations by minimizing the smallest eigenvalues of each cluster. The eigenvalues and eigenvectors of each cluster are related to the fault dimension and orientation, respectively. We extend the OADC method by incorporating high-quality source mechanisms of the earthquakes to specify seed planes rather than using randomly-seeded planes. Our fault models show a more complicated geometry than the simple three-faults model in previous studies, especially within the impact structure region, and support the along-strike variation in the fault dips suggested by recent study.

**1 Introduction**

The Charlevoix Seismic Zone (CSZ) is located along the early Paleozoic St. Lawrence rift zone in southeastern Quebec at the location of a major Devonian impact structure. The impact structure superimposed three major basement faults trending approximately N35°E. The three major rift faults in the CSZ are the Gouffre Northwest Fault, Saint-Laurent fault, Charlevoix Fault (Powell and Lamontagne, 2017; Fadugba et al., 2019). CSZ is the most active seismic zone in the southwestern Canada (Anglin, 1984) and has housed large earthquakes, up to M6.5 in 1925 (Bent, 1992) and M7.5 in 1663 (Ebel, 2011). The CSZ poses higher risks due to its history of generating M4+ earthquakes compared to the other seismic zones in the area and its proximity to densely populated cities (e.g.

47 Quebec City, Ottawa and Montreal). Other seismic zones in Eastern Canada are the Lower  
 48 St. Lawrence (LSL), Ottawa-Bonnechere graben (OBQ), Western Quebec seismic zone  
 49 (WQ) and the Saguenay graben (SG) (Fig. 1, Baird, McKinnon, and Godin (2010)).

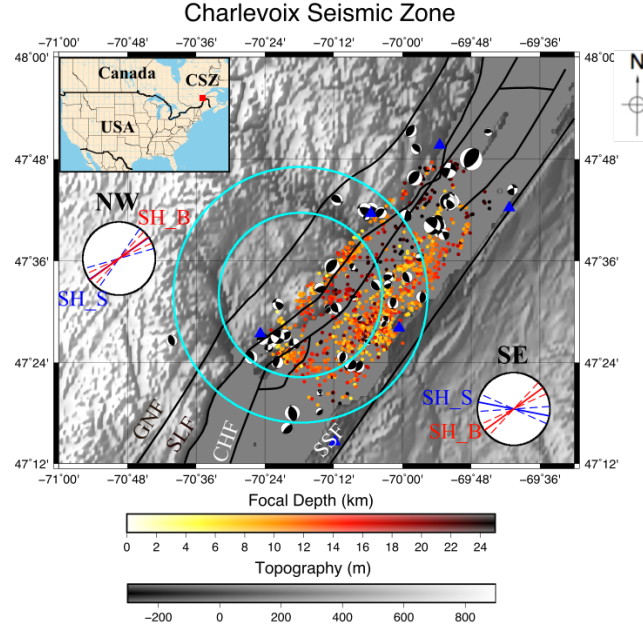


**Figure 1.** Topography and seismicity of the Charlevoix Seismic Zone (CSZ) showing the location of the impact structure and the seismic stations (blue triangles) (Modified after Fadugba et al., 2019). The locations of the impact structure is represented with the outer cyan circle while the more damaged inner impact structure as the inner cyan circle. Small circles are the relocated epicenters (Powell & Lamontagne, 2017) and their colors represent the focal depths. The focal mechanisms are for the earthquakes used by Mazzotti and Townend (2010) for the stress inversion of focal mechanism ( $SH_S$ ) and from borehole breakout measurements ( $SH_B$ ) for the earthquake clusters northwest and southeast of the crater center. Solid black lines mark the rift faults known in the region: GNF, Gouffre Northwest Fault; SLF, Saint-Laurent fault; CHF, Charlevoix Fault; and SSF, South Shore Fault (Lamontagne, 1999; Rondot, 1971). The inset shows the location of the CSZ in eastern Canada. Earthquake epicenters are from the National Resources Canada catalog for the years 1988-2011.

50 Powell and Lamontagne (2017) determined 3D  $V_p$  and  $V_s$  velocity model of the  
 51 CSZ, and relocated the earthquakes using the 3D velocity model. Visual estimation of  
 52 the epicenters in the CSZ shows two major earthquake clusters: the northwestern (NW)

53 and southeastern (SE) clusters. The NW clusters have earthquakes on the Gouffre Northwest  
54 fault while the SE clusters comprise of the earthquakes on the Saint-Laurent and  
55 Charlevoix faults (Fig. 1). Powell and Lamontagne (2017) also observed circular arcs of  
56 seismicity that follow the edge of the impact structure found in 3D tomographic inves-  
57 tions. The presence of damaged crustal crust from the impact crater makes the CSZ an  
58 anomalous seismic zone. The presence of the impact crater should decreased the seis-  
59 micity of the CSZ due to the damaged crustal rocks (Solomon et al., 1987).

60 Previous studies observed a unique distribution of earthquakes in the CSZ (e.g. Baird  
61 et al., 2010) and a stress rotation in the CSZ relative to the regional first-order maxi-  
62 mum horizontal stress rotation (Zoback, 2010 Mazzotti and Townend, 2010). The M4+  
63 earthquakes in the CSZ are concentrated outside the crater, but on the major rift faults,  
64 while the small-magnitude earthquakes are located within and beneath the crater region.  
65 Despite the high level of seismicity in the CSZ, only a few earthquakes are located on  
66 the southwestern part of the crater region (Fig. 1). In addition to the unique distribu-  
67 tion of earthquakes in the CSZ, Mazzotti and Townend (2010) observed a significant clock-  
68 wise rotation in the horizontal stress orientation derived from focal mechanisms relative  
69 to the first-order regional stress orientation. Within the CSZ, stress inversion of focal  
70 mechanisms of the earthquakes on the NW cluster aligns with the first-order regional  
71 stress orientation while that of the southeastern cluster shows a significant clockwise ro-  
72 tation relative to the NW cluster (Mazzotti and Townend, 2010).

73 Numerical modeling gives insight into the earthquake distribution and stress ro-  
74 tation in the CSZ (e.g. Baird et al., 2010, Hurd and Zoback 2012, Fadugba et al., 2019).  
75 However, these numerical models require a realistic but simplified fault geometry due  
76 to the sensitivity of the modeled stress on the fault geometry. Previous work suggests  
77 two sets of geometries for the rift faults in the CSZ. One set has a uniform dip of 70°SE  
78 for all three faults (e.g. Baird et al., 2010), while the second set has 65°, 40°, and 40°SE,  
79 from north to south, respectively (Powell and Lamontagne, 2017). Fadugba et al. (2019)  
80 used the two fault geometries to model the stress state of the CSZ. Fadugba et al. (2019)  
81 observed a partial success of modeled stress concentrations in each two fault geometries  
82 in explaining the observed seismicity and stress rotations, which might suggests along-  
83 strike variations in the dip angles of the rift faults. Visual estimation of fault planes from  
84 over 1300 relocated hypocenters in the CSZ (Powell and Lamontagne, 2017) suggests more

85 complex fault geometry. An important research topic is whether pattern recognition al-  
86 gorithm can be used to determine simplified and realistic fault geometry in the CSZ.

87 Several work has been done to determine realistic fault planes from the cloud of  
88 hypocenters. For example, Ouillon et al. (2008) developed an Optimal Anisotropic Dy-  
89 namic Clustering (OADC) analysis technique to delineate fault planes within the after-  
90 shocks of the Parkfield earthquake sequences. The OADC method is a pattern recogni-  
91 tion method aimed to reconstruct fault networks using the covariance of the spatial dis-  
92 tribution of earthquakes from seismic catalogs. Ouillon and Sournette (2011) used the  
93 Guassian kernel in a EM method to identify fault planes in intersecting cloud of seismic-  
94 ity, hence intersecting fault planes. Wang et al. (2013b) extended the OADC method  
95 to develop Anisotropic Clustering of Location Uncertainty Distributions (ACLUD). The  
96 new ACLUD method incorporates some validation steps in order to give the best agree-  
97 ment between the fault planes from a method similar to OADC to the observed focal mech-  
98 anisms. They also used the uncertainty in the location of each earthquake in the cat-  
99 alog instead of the threshold value assumed in Ouillon et al. (2008). The validation steps  
100 proposed by Wang et al. (2013) produce several fault geometries that need the user's judg-  
101 ment for discrimination.

102 Based on the assumption that modern seismicity in the CSZ illuminates active faults,  
103 I will incorporate focal mechanisms to the Optimal Anisotropic Dynamic Clustering (OADC)  
104 algorithm to determine realistic fault planes in the CSZ (Ouillon et al., 2008). I employ  
105 a couple of hypotheses in this research. The first hypothesis is that modern seismicity  
106 in the CSZ illuminates active faults and can be used to determine the number of the faults,  
107 geometries and the interconnectivity of the fault system. The interconnectivity of these  
108 faults can be used to predict the maximum magnitude earthquake in the CSZ (Harris  
109 et al., 1991; Harris and Day, 1993). If modern earthquakes occur on active faults, then  
110 the focal mechanisms of these earthquakes can be used to determine the style of fault-  
111 ing e.g. strike-slip or reverse faulting. In other words, earthquake source mechanisms and  
112 seismicity clusters define coherent fault surfaces, hence, the observed slip directions im-  
113 plied by the mechanisms should also be coherent. Based on observed circular arcs of seis-  
114 micity that follow the edge of the impact structure found in 3D tomographic inversions  
115 (Fig. 1, Powell and Lamontagne, 2017), the second hypothesis is that the interface be-  
116 tween the crater and the crust can slip and thus can cause earthquakes. High-resolution  
117 focal mechanisms of moderate earthquakes (M2 – M4) will then be coupled with the Op-

118 timal Anisotropic Dynamic Clustering (OADC) analysis technique to delineate realistic  
 119 fault geometries. The derived fault geometry from this study will be incorporated in  
 120 future geodynamic models to determine if the modeled stress result is consistent with  
 121 the regional stress field and hence provide an explanation for the seismicity of CSZ.

## 122 2 Methods

123 We use the relocated hypocenters of Powell and Lamontagne (2017) in this study.  
 124 Powell and Lamontagne (2017) relocated the hypocenters, to an error of less than 1 km,  
 125 using the 3-D V<sub>p</sub> and V<sub>s</sub> velocity models determined from a travel time tomography study.  
 126 Specifically, the hypocenters were relocated with horizontal and vertical errors of 0.15  
 127 km and 0.35 km, respectively. Despite the high precision in hypocenter location, the hypocen-  
 128 ter shows some unclustered hypocenter probably due to the damaged crustal rocks in  
 129 the impact structure (Fig. 1).

130 The method used in this study can be broadly divided into two subsections. We  
 131 first perform declustering analysis on the catalog to remove isolated and diffused earth-  
 132 quakes, in order to highlight the rift faults in the CSZ. Based on the diffuse nature of  
 133 the background seismicity recorded in the CSZ, the seismicity in the CSZ will be sep-  
 134 arated into clustered and unclustered events based on the collapsing method (Jones and  
 135 Stewart, 1997) and cumulative tetrahedra volume (Ouillon and Sornette, 2011). We then  
 136 apply an Optimal Anisotropic Dynamic Clustering (OADC) algorithm to model realis-  
 137 tic fault planes that best fit the hypocenter data.

138 In order to avoid spurious fault plane identifications, each cluster of events will be  
 139 isolated before determining optimal fault planes that minimize the thickness of the clus-  
 140 ter. This is necessary because the OADC method will tend to fit the hypocenters with  
 141 a near-horizontal plane when the depth extent of the earthquakes in a cluster is far less  
 142 than the areal extent of the cluster.

### 143 2.1 Declustering analyses

144 We used two techniques to decluster the hypocenters: a collapsing method (Jones  
 145 and Stewart, 1997) and the cumulative distribution of tetrahedra volume method (Ouil-  
 146 lon and Sornette, 2011). The collapsing method involves moving each hypocenter within  
 147 its uncertainty ellipsoid making the collapsed hypocenters within acceptable error in the

148 earthquake location algorithm. The error ellipsoid is constructed with 99.86% confidence  
 149 interval (i.e., 4 standard deviations). The idea of the cumulative distribution of tetra-  
 150 hedra volume method is that the volume of a tetrahedral formed by four neighboring hypocen-  
 151 ters of unclustered/isolated hypocenters will be higher than those of a clustered hypocen-  
 152 ter. Given the small horizontal and vertical errors in the relocation catalog, and the dif-  
 153 fuse nature of the seismicity, the cumulative distribution method has little success in sep-  
 154 arating the clustered hypocenters. To solve this problem, we first applied the collaps-  
 155 ing method on the catalog to reduce the variance of the earthquake distribution. and  
 156 then apply the cumulative distribution method to remove any remaining isolated/unclustered  
 157 hypocenters.

158 The collapsing method involves two loops: the first is on each hypocenter  
 159 while the other loop is on each generation of collapsed hypocenters. We encourage the  
 160 reader to see Jones and Stewart (1997) for more detailed description and limitations of  
 161 the method. In summary, the collapsing method involves the following steps: (1) For each  
 162 earthquake (object earthquake), we find all other earthquakes whose locations lie within  
 163 the error ellipsoid of the object earthquake using  $(\frac{x-x_0}{\sigma_x})^2 + (\frac{y-y_0}{\sigma_y})^2 + (\frac{z-z_0}{\sigma_z})^2 \leq s$ ,  
 164 where  $s$  is related to the confidence interval at the specified degree of freedom. In this  
 165 study, we use degree of freedom of 3, since the location of the hypocenters are in 3 di-  
 166 mension. (2) Determine the centroid of the earthquakes including the object earthquake,  
 167 and determine the distance and direction of the centroid to the object earthquake. We  
 168 then move the object earthquake by a factor of 0.68103 of the distance and in the direc-  
 169 tion to the calculated centroid (Press et al., 1986). The 0.68103 is necessary for stabil-  
 170 ity (Jones and Stewart, 1997). The location of the object earthquake remains unchanged  
 171 during this iteration, so the order the hypocenters are processed does not affect the re-  
 172 sult.

173 The outer loop of the collapsing method involves statistical assessment of the move-  
 174 ment of the hypocenters, using the following steps: (1) We store the new location of the  
 175 hypocenters as a new generation of hypocenters. (2) We normalized the movement of  
 176 object earthquake by corresponding standard deviation, and (3) compare the distribu-  
 177 tion of the normalized movement with a theoretical chi distribution with degree of free-  
 178 dom of 3. We used chi distribution instead of chi-square distribution because the move-  
 179 ment of the hypocenters have been normalized by standard deviation. we then repeat  
 180 the collapsing method for the next generation of collapsed hypocenters while the loca-

181 tions and sizes of the ellipsoids of uncertainty of the original hypocenter locations remain  
 182 unchanged.

183 We then apply a cumulative distribution of tetrahedra volume method on the col-  
 184 lapsed hypocenters to remove unclustered hypocenters. We compare the distribution of  
 185 the volumes of the tetrahedra in the collapsed (natural) catalog to the distribution of  
 186 tetrahedra formed from randomized hypocenters (catalog) in a domain similar to the nat-  
 187 ural catalog. We generate the randomized catalog by randomizing the x, y and z coor-  
 188 dinate of each hypocenter in the collapsed catalog. We randomized the hypocenter in  
 189 depth as well because of the high number of hypocenters in the upper 15 km thus affect-  
 190 ing the distribution of the tetrahedra volume in the randomized catalog. Ouillon and Sor-  
 191 nette (2011) did not randomize the depth of the natural catalog. Following (Ouillon and  
 192 Sornette, 2011), the cumulative distribution can be summarized as follows. (1) Deter-  
 193 mine the volume ( $V$ ) of tetrahedra formed with quadruplets of nearest neighbor events  
 194 around each hypocenter using equation (1) for both the collapsed ( $V$ ) and randomized  
 195 ( $V_0$ ) catalogs. An apparent challenge occurs when the four nearest neighbor of an iso-  
 196 lated hypocenter are clustered. Hence, we used three surrounding hypocenters and the  
 197 object earthquake to form the tetrahedra. (2) We determine the cumulative distributions  
 198 of the volumes, i.e.,  $N(V)$  and  $N_0(V_0)$ . (3) We determine the volume ( $V_0$ ) of the random-  
 199 ized catalog corresponding to 5% quantile of the distribution, i.e., probability of 0.05.  
 200 (4) We then remove all hypocenters in the natural catalog with  $V > V_0$ , under the as-  
 201 sumption that the correlated hypocenters in the collapsed catalog have volumes smaller  
 202 than the 5% quantile of the tetrahedra volume distribution in the randomized catalog.

$$V = \frac{1}{6} \times \begin{vmatrix} x_1 & y_1 & z_1 & 1 \\ x_2 & y_2 & z_2 & 1 \\ x_3 & y_3 & z_3 & 1 \\ x_4 & y_4 & z_4 & 1 \end{vmatrix} \quad (1)$$

## 203 2.2 Modified OADC algorithm

204 Ouillon et al., (2008) developed the OADC method to determine an optimal num-  
 205 ber of clusters. OADC method is a generalization of the k-means method using randomly-  
 206 seeded planes to partition hypocenters into clusters. In this algorithm, we set the min-  
 207 imum ( $N_0$ ) and maximum ( $N_{\max}$ ) number of faults to use in the clustering analysis, in

addition to the maximum cluster thickness ( $\Delta$ ) allowed in the algorithm. The value of  $\Delta$  should be the same order of magnitude as the maximum radius of uncertainty ellipsoid of the hypocenters.

The algorithm starts with  $N_0$  fault with random positions, orientations, and sizes. The value of  $N_0$  is one in this study. In this study, we set the  $N_0$ ,  $N_{\max}$  and  $\Delta$  to one, five and 0.5 km, respectively. We chose a  $N_{\max}$  value of five to account for any along-strike variation of dip angles in the crater region (Fadugba et al., 2019). We partition each hypocenter into different clusters based on its distance to the fault(s). We then determine the covariance matrix ( $\mathbf{C}$ , equation 2) of each cluster. The idea of the algorithm is to iteratively determine optimal fault planes that minimize the maximum eigenvalues of the covariance matrix. We perform a principal component analysis on the covariance matrix of each cluster to determine its eigenvectors and eigenvalues. Under the assumption that earthquakes are uniformly distributed over a fault plane, we infer the fault length, width, and thickness from the eigenvalues and the corresponding eigenvectors (Ouillon et al., 2008). This analysis is repeated until the algorithm converges to a fixed geometry. The computation stops when the maximum value of  $\lambda_3$  in all the clusters is less than the value of  $\Delta$ .

$$\text{Covariance matrix, } \mathbf{C} = \begin{pmatrix} \sigma_x^2 & cov(x, y) & cov(x, z) \\ cov(x, y) & \sigma_y^2 & cov(y, z) \\ cov(x, z) & cov(y, z) & \sigma_z^2 \end{pmatrix} \quad (2)$$

According to Ouillon et al., 2008, we attribute the largest eigenvalues ( $\lambda_1$ ) to the length of the cluster, and the azimuth of the corresponding eigenvector to represent the strike of the fault. In addition, we use the intermediate ( $\lambda_2$ ) and smallest ( $\lambda_3$ ) eigenvalues to infer the width and thickness of the fault planes, respectively. The barycenter of each cluster (e.g.,  $x_b = \text{mean}(x)$ ) coincides with the center of the fault. Based on a statistical method, Ouillon et al., (2008) estimated the length (L) and width (W) of the fault plane using  $\lambda_1\sqrt{12}$  and  $\lambda_2\sqrt{12}$ , respectively. The value of  $\lambda_3$  gives information on the thickness of the cluster. The strikes and dips of the fault planes are determined from the eigenvector of the minimum eigenvalue ( $\lambda_3$ ) of each cluster.

However, if the maximum  $\lambda_3$  in the stable fault geometry is greater than  $\Delta$ , the fault in thickest cluster is replaced by at least two new faults with random locations and

236 orientations within the cluster. The lengths of the new faults are one-half that of the orig-  
 237 inal thick fault. We perform the splitting process several times (20 times in this study)  
 238 to determine the random fault geometry that gives the least maximum  $\lambda_3$  at the result-  
 239 ing fixed geometry. The number of fault increases by one, and the covariance matrix anal-  
 240 ysis is repeated. The simulation stops when the value of  $\lambda_3$  is less than the value of  $\Delta$ ,  
 241 or the  $N_{\max}$  is reached.

242 In this study, we incorporate the focal mechanisms into the OADC algorithm to  
 243 split the 'thick' cluster instead of using a randomly-seeded planes. We use any available  
 244 high-quality focal mechanisms of earthquakes that are within or at a distance of 1 km  
 245 to the thick cluster. We assign the first two dominant strike direction of the focal mech-  
 246 anisms and the average of their corresponding dips to two faults. Wang et al., 2013 also  
 247 incorporate focal mechanisms to OADC in their the ACLUD method, but as a valida-  
 248 tion step after determining several results from OADC-type algorithm.

249 The idea is to plot the nodal plane normal vectors for earthquakes with high-quality  
 250 source mechanisms and use the dominant orientations to specify the planes in the OADC  
 251 method rather than using randomly-seeded planes.

### 252 3 Results

#### 253 3.1 Declustering analyses

##### 254 3.1.1 Modified collapsing method

255 The relocated hypocenters shows a thicker cloud of seismicity about the rift faults  
 256 and some earthquakes appear to rim around the impact structure (Fig. 2C).

255 **Figure 2.** (A) Relocated earthquake distribution of the CSZ (Powell and Lamontagne, 2017),  
 256 and (B) a theoretical scaled chi distribution.

257 In order to reduce the thickness of the clusters, we applied the collapsing method  
 258 to account for the location errors in the hypocenters (Jones and Stewart, 1997). Figure  
 259 – and – show the result of the collapsing method at 10th and 20th iteration, respec-  
 260 tively, and the normalized movement of each hypocenter relative to its original location.

**Figure 3.** (A) Collapsed earthquake distribution at iteration number 10, and (B) the movement of the hypocenters compared with the theoretical scaled chi distribution.

**Figure 4.** Same as figure – but at an iteration number of 20.

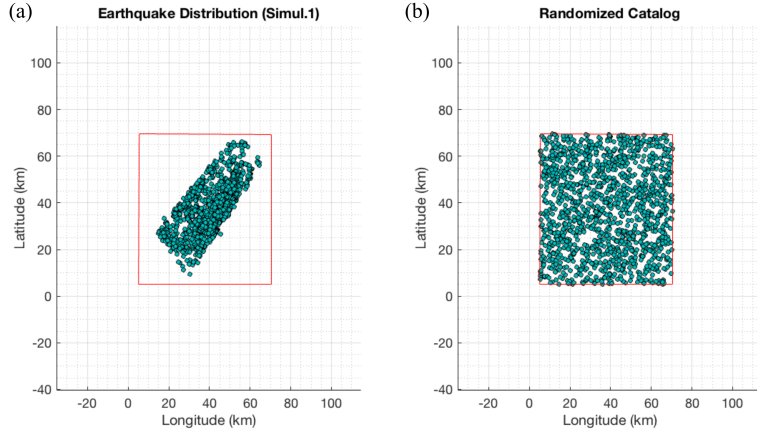
The collapsing method has clustered some of the hypocenters. We stopped the iteration at 20 even though the hypocenter movements has not fitted the theoretical chi distribution. This is because the objective of collapsing method in this study is to reduce the variability in the hypocenter location, and not to totally collapse the hypocenters. The collapsing method at higher iterations and higher scaling factors of the uncertainty ellipsoid collapsed the earthquakes on a a rift fault to a line thereby affecting its depth information significantly. This may be due to the higher standard error in he z-direction.

We then applied the cumulative distribution method on the collapsed catalog to remove some of the hypocenters that are isolated.

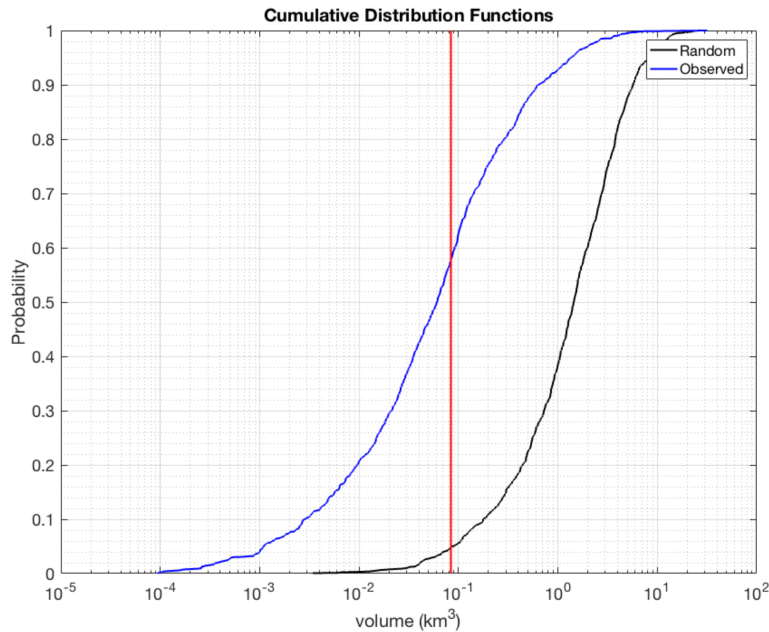
### 3.1.2 Cumulative distribution of tetrahedra volume

We determine the volume of the tetrahedra for each earthquake in the 3D joint relocation of the 1329 earthquakes in the CSZ (Fig. 2A, Powell and Lamontagne, 2017). We first generated the randomized catalog within the domain size similar to the seismic zone (Fig. ). The volumes of the tetrahedra ranges from  $10^{-20}$  to about  $31.61 \text{ km}^3$ . The very small lower bound of the volumes is because of the earthquakes that are co-located due to the collapsing method. We clipped the lower bound of the tetrahedra volumes at  $10^{-5} \text{ km}^3$  (Fig. ). The tetrahedra volume in the randomized catalog ranges from 0.0015 to  $31.05 \text{ km}^3$ . The similarity in the maximum tetrahedra volume further supports the need to apply collapse method before the cumulative distribution of tetrahedra volume.

We determine the cumulative distribution function (CDF) of the tetrahedra volume of both catalogs (Fig. 3). The volume at 5 percent probability ( $V_{05}$ ) is  $0.099 \text{ km}^3$  and the probability at target volume ( $N(V_{05})$ ) = 0.7223. This method removes 370 unclustered earthquakes (27.84% of the original catalog). Figure 2B shows the collapsed and clustered hypocenters while figure 2C shows highlights the unclustered hypocenters.



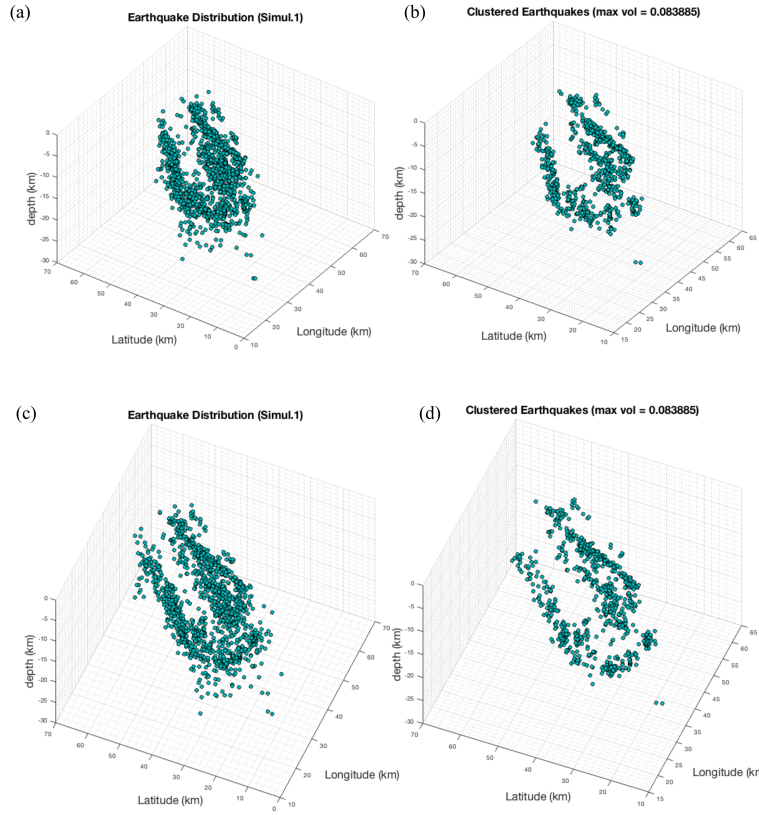
**Figure 5.** Domain of randomized catalog.



**Figure 6.** cumulative distribution curve for hypocenters of the earthquakes of the CSZ.

The clustered and unclustered hypocenters give interesting incite to the seismicity of the CSZ. For example, the clustered hypocenters occur on identifiable alignment related to the main rift faults in the CSZ, and have been enhanced compared to the full relocated hypocenters of Powell and Lamontagne (2017) (compare figures 2A and 7B). The clustered earthquakes also reveal a curvature of hypocenters in the western part of the seismicity distribution probably following the boundary of the crater. The unclustered earthquakes are random showing no significant alignment which may depict con-

293 concentration of hypocenters on rift faults (Fig. 2D). However, the unclustered earthquakes  
 294 are more in the impact structure than on those near the rift faults.

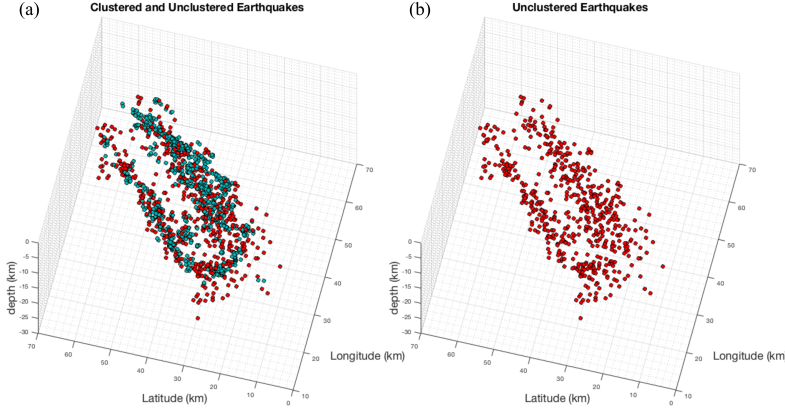


**Figure 7.** Clustering of earthquakes in CSZ using modified cumulative distribution method.

### 3.2 Fault plane geometry of the CSZ

296 The best-fit fault planes from the modified OADC algorithm are geologically fea-  
 297 sible (Fig. 6). Figures 6A and 6B show the intermediate fault models using 1 and 3 fault  
 298 planes, respectively. The one-fault intermediate model fit the clustered hypocenter but  
 299 with a large minimum eigenvalue compared to the input threshold (0.001 km) (Fig. 6A).  
 300 The fault was splitted, the OADC algorithm is repeated. When the number i faults is  
 301 3, the OADC algorithm was fitted one fault to the NW and SE clusters, and also fitted  
 302 the earthquakes beneath the crater with a near-horizontal fault (Fig. 6B).

303 The best fit occur when the number of faults is 5 (Fig. 6C and D). The OADC fit-  
 304 ted the SE cluster with two fault planes with dips  $43.9^\circ$  and  $42.8^\circ$ , respectively. The NW

**Figure 8.** Unclustered hypocenters.**Table 1.** Fault geometry of the CSZ using OADC method.

Fault No	Strike	Dip	Possible mapped fault
1	65.8°	43.9°	Saint-Laurent fault
2	56.4°	42.8°	Charlevoix fault
3	82.1°	33.5°	Crater boundary
4	30.3°	34.8°	Crater boundary
5	50.0°	60.0°	Gouffre Northwest fault

305 cluster was fitted with a steeper faults with a dip of 60°. Within the crater region, OADC  
 306 fitted two more faults with shallower dips: 33.5° and 34.8°. The shallower dip planes are  
 307 probably in response to the earthquakes wrapping around the crater region. Table 1  
 308 shows the summary of fault geometry from the OADC algorithm.

## 309 4 Discussion

310 In this section, we will discuss the unclustered and clustered hypocenters, and the  
 311 limitations of the OADC from this study.

### 312 4.1 Unclustered seismicity

313 *The removal of the Unclustered seismicity decrease the fuzziness of earth-  
 314 quake distribution in the CSZ, thereby highlighting the rift faults (Figs. 2A*

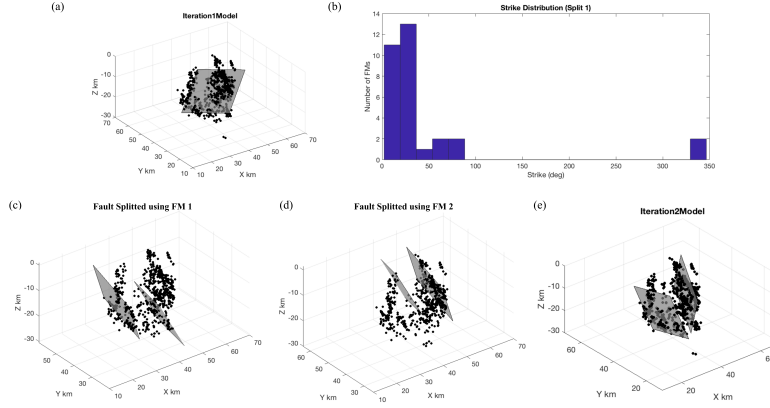


**Figure 9.** Intermediate fault models of OADC method on the clustered earthquakes.

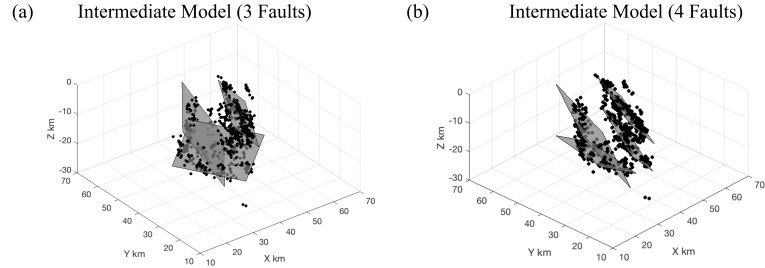


**Figure 10.** Intermediate fault models of OADC method on the clustered earthquakes.

315     **and C).** The unclustered earthquakes do not have inherent structure showing the rift  
 316     faults, which suggests that they do not occurred on the major rift faults in the CSZ. The  
 317     lack of inherent alignment validate the declustering method has not removing clustered  
 318     hypocenters. Powell and Lamontagne (2017) also shows that the rift faults can not be  
 319     traced inside the crater region. In this method removes the fuzziness of the seismicity  
 320     within the crater and thus, the faults can be followed all the crater within the crater re-  
 321     gion. Thereby, helps to constrain the geometry of the rift faults (Fig. 2C).

322     *The unclustered seismicity in the crater region shows the geometry of  
 323     the crater (Figs. 2B and D).* The unclustered seismicity in the crater region is the  
 324     background seismicity, and is mainly within the crater region. These background seis-  
 325     micity highlights the damaged region of the crater (the inner circle in Figure 1). *Cre-*  
 326     *ate a 3D map of the removed seismicity to highlight the geometry of the crater.*

327     *Figure of the background seismicity showing the inner circle.*

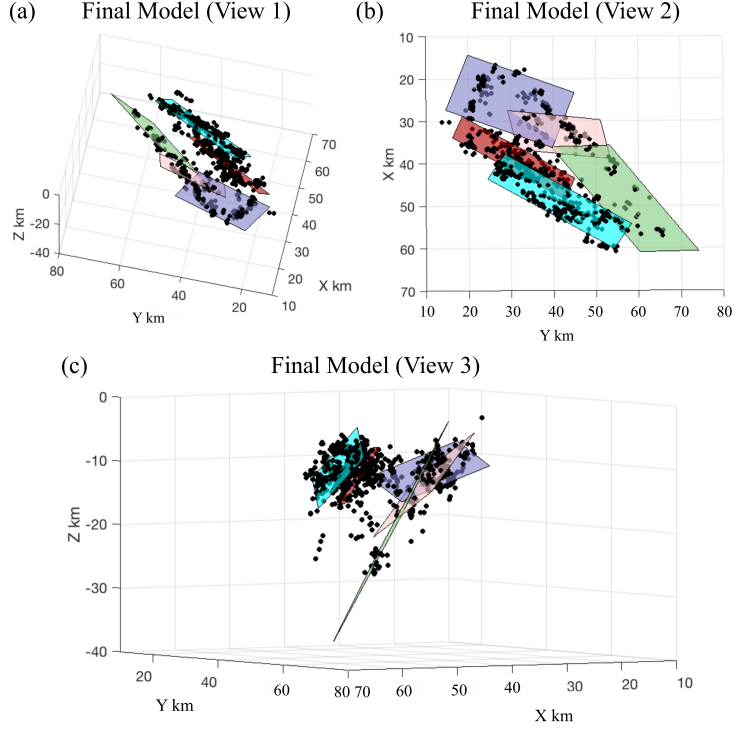


**Figure 11.** Final fault models of OADC method on the clustered earthquakes.

328

## 4.2 Clustered seismicity

329

*The clustered seismicity show identifiable planes revealing the geo-*

330

*metry of the three major rift faults in the CSZ (Fig. 3D).* The first fault dips at

331

an angle of 60° while the other two main rift faults dip at 44° and 43°, respectively (Fig.

332

4D). We need to plot the clustered earthquakes on a geologic map to see the difference.

333

And also plot some cross-sections. The results from this study also support Powell and

334

Lamontagne (2017) that the alignment of the earthquakes on identifiable planes suggests

335

that the earthquakes occurred on the rift faults instead of concentrating within the fault

336

volume as suggested by previous authors (e.g. Baird et al. 2010, Auglin, Lamontagne,

337

Rondot). These fault geometries match the work by Powell and Lamontagne (2017). The

338

rift faults in the OADC supports that the South Shore fault do not play a role in the seis-

339

micity of the CSZ.

340

*In addition to the simple geometry of the rift faults, the seismicity re-*

341

*veals a more complicated geometry (Fig. 4D). There is a change in the strike*

342

*of the rift faults.* Similar to what we see on the fault trace on Figure 1. Within the

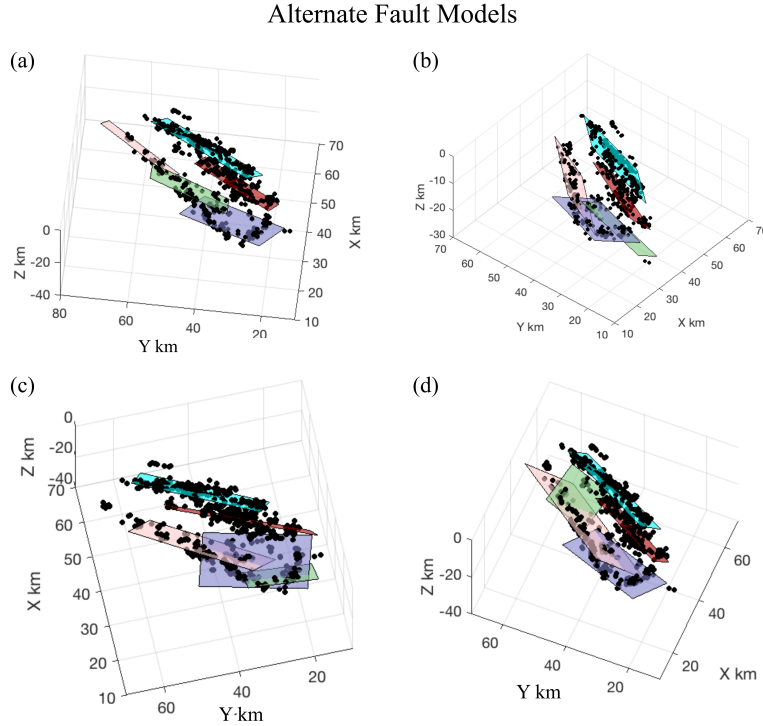


**Figure 12.** Alternate fault models of OADC method.

343 crater region, the faults are farther apart and somewhat converge in the northeastern  
 344 part of the seismic zone. The middle and Charlevoix fault are closer outside the crater  
 345 region. This is contrary to the simple fault geometry employed in Fadugba et al. (2010)  
 346 with constant distance separation between the rift faults.

347 *And also reveals a change of dip in the first rift faults (Fig. 3D).* in the  
 348 form of three segments. Outside the crater, the first rift fault follow the first order strikes  
 349 of the rift faults. Along strike variation in the dip of the rift faults (Fadugba et al., 2019).  
 350 Within the crater region, the faults dips at  $33.4^\circ$  and  $34.8^\circ$ .

351 *The seismicity follows the crater boundary (Fig. 3D).* especially well in the  
 352 northeastern part of the crater, and the shows that the seismicity also wrap around and  
 353 beneath the crater. This seismicity highlights the geometry of the crater thereby con-  
 354 straining the depth of the crater.

355 Lambda3 is better to solve fitting horizontal plane fit. Show two figures showing  
 356 fit with both lambda3 and global variance.

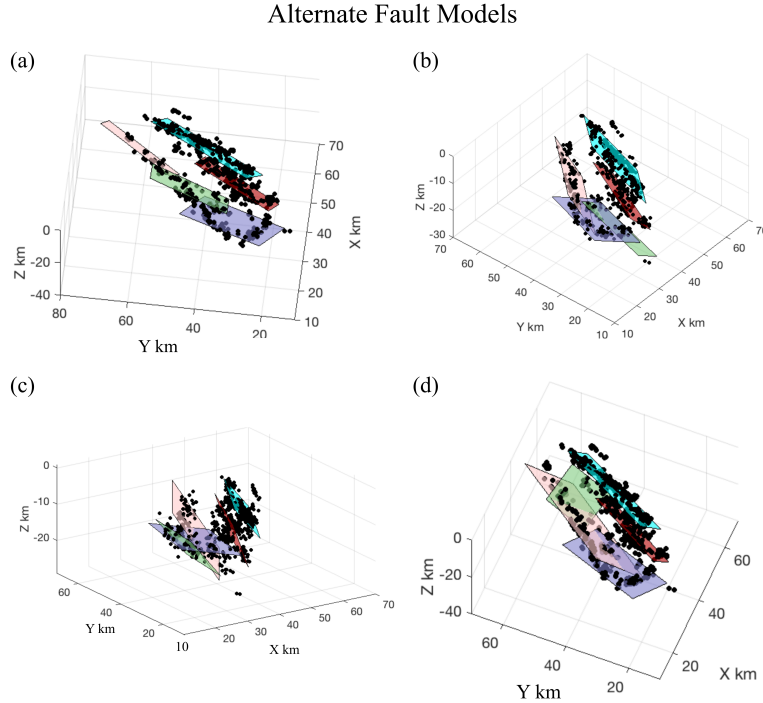


**Figure 13.** Alternate fault models of OADC method.

357

### 4.3 Limitation of OADC

358

*The results of OADC algorithm may change for every run* because the results depend on the initially random seed planes within each cluster. Therefore, we may need to repeat the algorithm several time until the fault geometry is geologically feasible.

359

360

361

362

363

*The surface projection of the fault planes from OADC may not coincide the fault trace* on the geologic map. We need to find out how it changes.

364

## 5 Conclusions

365

The first fault dips at an angle of  $60^\circ$  while the other two main rift faults dip at  $44^\circ$  and  $43^\circ$ , respectively. These fault geometries match the work by Powell and Lamontagne (2017). The rift faults show a more complicated geometry than the simple three-faults model in previous works, especially within the crater region. Within the crater region, the faults dips at  $33.4^\circ$  and  $34.8^\circ$ .

366

367

368

369

370      **Acronyms**

371      **CSZ** Charlevoix Seismic Zone

372      **SH<sub>max</sub>** Maximum horizontal principal stress

373      **OADC** Optimal Anisotropic Dynamic Clustering

374      **ACLUD** Anisotropic Clustering of Location Uncertainty Distributions

375      **CDF** Cumulative Distribution Function

376      **Acknowledgments**

377      This research was supported by Center for Earthquake Research and Information, Uni-  
378      versity of Memphis.

379      **References**

380      Anglin, F. (1984). Seismicity and faulting in the Charlevoix zone of the St. Lawrence  
381      Valley. *Bulletin of the Seismological Society of America*, 74 (2): 595–603.

382      Baird, A. F., McKinnon, S. D., & Godin, L. (2010, nov). Relationship between  
383      structures stress and seismicity in the Charlevoix seismic zone revealed by 3-D  
384      geomechanical models: Implications for the seismotectonics of continental inte-  
385      riors. *Journal of Geophysical Research*, 115(B11). doi: 10.1029/2010jb007521

386      Bent, A. L. (1992, 10). A re-examination of the 1925 Charlevoix, Québec, earth-  
387      quake. *Bulletin of the Seismological Society of America*, 82(5), 2097-2113.

388      Ebel, J. E. (2011, 6). A New Analysis of the Magnitude of the February 1663 Earth-  
389      quake at Charlevoix, QuebecA New Analysis of the Magnitude of the February  
390      1663 Earthquake at Charlevoix, Quebec. *Bulletin of the Seismological Society*  
391      of America, 101(3), 1024-1038. doi: 10.1785/0120100190

392      Lamontagne, M. (1999). Rheological and geological constraints on the earthquake  
393      distribution in the Charlevoix Seismic Zone, Quebec, Canada. *Geological Sur-*  
394      *vey of Canada. Open File, D3778.*

395      Mazzotti, S., & Townend, J. (2010, apr). State of stress in central and eastern North  
396      American seismic zones. *Lithosphere*, 2(2), 76–83. doi: 10.1130/l165.1

397      Powell, C. A., & Lamontagne, M. (2017, aug). Velocity models and hypocenter  
398      relocations for the Charlevoix Seismic Zone. *Journal of Geophysical Research:*  
399      *Solid Earth*, 122(8), 6685–6702. doi: 10.1002/2017jb014191

- 400 Rondot, J. (1971, aug). Impactite of the Charlevoix Structure Quebec,  
401 Canada. *Journal of Geophysical Research*, 76(23), 5414–5423. doi:  
402 10.1029/jb076i023p05414  
403 Rondot, J. (2000). Charlevoix and sudbury as gravity-readjusted impact struc-  
404 tures. *Meteoritics & Planetary Science*, 35(4), 707-712. doi: 10.1111/j.1945  
405 -5100.2000.tb01454.x